Ceramics International 48 (2022) 540–547

Contents lists available at ScienceDirect

Ceramics International

journal homepage: www.elsevier.com/locate/ceramint

Hard and electrically conductive multicomponent diboride-based films with high thermal stability

A. Farhadizadeh, J. Vlček *, J. Houška, S. Haviar, R. Čerstvý, M. Červená

Department of Physics and NTIS, European Centre of Excellence, University of West Bohemia, Univerzitni 8, 30614, Plzen, Czech Republic

ARTICLE INFO

Keywords:
Multicomponent diborides
High-entropy diborides
Thermal stability
Low compressive stress
Hardness
Electrical conductivity

ABSTRACT

We report high-quality, hard (31–41 GPa), crack-resistant (hardness-to-effective Young's modulus ratio of 0.13–0.16) and electrically conductive (2.8–4.2 × 10^5 S m^{-1}) HfB_2-based ceramic materials with high thermal stability. The materials were prepared in the form of well adhesive films using a simple deposition process: pulsed magnetron sputtering (B_4C target overlapped by metal stripes) onto floating substrates. We go through a wide range of compositions resulting from incorporating five other metals (Ti, Y, Zr, Ho or Ta) which partially replace Hf, and focus on the effect of the number and characteristics of elements in the metal sublattice. Regardless of the number of incorporated elements, no segregation to more than one AlB_2-type crystalline phase was observed. Growing number of metal elements leads to decreasing crystal size as indicated by the width of diffraction peaks, strongly decreasing compressive stress to less than 2 GPa and slightly decreasing hardness and electrical conductivity. The experimental data are explained by Monte-Carlo calculations of the energy delivered into the growing films. The thermal stability of septenary diboride-based films $Hf_8Zr_4Ti_4Ta_4Y_5B_{60}C_9$ and $Hf_{10}Zr_4Ti_4Ta_4Ho_5B_{58}C_9$ was superior to that of quaternary films $Hf_{22}Y_5B_{58}C_9$ and $Hf_{22}Ho_5B_{58}C_9$ when annealed to 1300 °C. Both the single solid solution crystalline phase (X-ray diffraction) and the dense and pinhole-free structure (scanning electron microscopy) were observed for the septenary films not only before but also after annealing. The results are important for the design and industry-friendly preparation of thin-film materials combining multiple functional properties for various technological applications.

1. Introduction

Diboride-based materials crystallizing in the AlB_2-type structure possess exceptional properties including ultra-high melting point (typically more than 3000 °C), high hardness (over 20 GPa) and high electrical conductivity (metal-like behavior) [1,2]. In parallel, these materials constitute an important class of ultra-high temperature ceramics (UHTCs) due to their thermal stability and potential use at elevated temperatures [3,4]. Many studies have been conducted to explore/improve the properties of these materials in the bulk form (see e.g. Refs. [5–7] for recent reviews) as well as in the form of films. The latter includes binary diboride coatings TiB_2 [8,9], ZrB_2 [3], TaB_2 [10], HfB_2 [11], diboride-based coatings Ti–B–C [12], Hf-B-Si-C [13,14], M-B-C-N (M = Ti, Zr, Hf) [15] or ternary diboride coatings $Zr_xTa_{1-x}B_y$ [16,17], $Zr_{1-x}Cr_xB_y$ [18], $Ti_{1-x}Ta_xB_{2\pm\Delta}$ [19].

Recently, multicomponent diborides with at least 5 metal elements in a high-entropy metal sublattice have been introduced and found to have promising properties [20]. Unlike binary diborides, there are only a few works dealing with high-entropy diboride films. Thermally stable solid solution $(Hf,Ta,V,W,Zr)B_2$ has been successfully deposited via magnetron sputtering with hardness over 40 GPa and thermal stability up to 1200 °C. However, an orthorhombic (V,W)B phase formed at higher temperatures [21]. In another work the comparison of $(Zr,Ti,Hf,V,Ta)B_2$ with $(ZrTi)B_2$ and ZrB_2 revealed its higher hardness in the as-deposited state but also higher affinity to oxygen when the temperature exceeds 1100 °C [22]. The entropic effect in high-entropy alloys is believed to increase the thermal stability of the compounds under certain conditions; moreover, high-entropy alloys can possibly benefit from sluggish diffusion, lattice distortion and cocktail effects [23].

However, there are open questions resulting from the following. First, one of the difficulties in the field of deposition of heavy metal diborides such as HfB_2 or TaB_2 is very high compressive stress (up to 10.5 GPa) [24–26] and the resulting delamination of films [27]. A case can be made that this high compressive stress has largely limited the number of studies on HfB_2 and TaB_2 thin films, despite the fact that their high-temperature bulk properties outperform those of other diborides

* Corresponding author.
E-mail address: vlcek@kfy.zcu.cz (J. Vlček).

https://doi.org/10.1016/j.ceramint.2021.09.131
Received 12 July 2021; Received in revised form 31 August 2021; Accepted 13 September 2021
Available online 14 September 2021

[5]. Second, the available literature on thermally stable diboride-based films is focused only on the optimization of mechanical properties, rather than on the optimization of several functional properties such as hardness and electrical conductivity in parallel.

The subject of this work is a successive replacement of Hf in HfB_2-based films by numerous qualitatively different elements ranging from a relatively similar metal (Ta) through lighter metals from the same group (Zr and Ti) to much larger metals leading to lattice distortion effects (Y and Ho). We explore the effect of the number of different elements in the metal sublattice (i.e. the role of entropy stabilization) in itself, and the role of specific characteristics (e.g. mass or atomic radius) of individual elements. The main aim is to identify composition(s) which exhibit a combination of high hardness, high electrical conductivity, high thermal stability and high adhesion to substrates resulting from a low compressive stress. The application potential is maximized by focusing only on combinations of properties which are achievable by a simple deposition technique (substrates at a floating potential).

2. Methodology

2.1. Materials preparation

The films were synthesized using a Balzers BAS 450PM sputtering system with a planar rectangular unbalanced magnetron (see Ref. [28]) and a stationary substrate holder. The films were deposited onto p-type Si (100) and 6H–SiC (0001) substrates using pulsed magnetron sputtering from a single composite target (127 × 254 mm^2) in pure Ar. The target was formed by a B_4C plate (6 mm thick) overlapped by 6 individual stripes (3 mm thick) made of Hf, Zr, Ti, Ta, Y and Ho with the same 2.5% fractions in the target erosion area. Let us emphasize the advantage of B_4C over pure B in terms of higher conductivity and consequently suppressed arcing. We present results achieved for the films prepared with the following 11 combinations of metal stripes at a fixed 6 × 2.5 = 15% metal fraction in the target erosion area (the number of Hf stripes is given by the number before Hf): 5HfZr, 5HfTi, 5HfY, 5HfHo, 4HfZrTi, 4HfZrY, 4HfZrHo, 3HfZrTiY, 3HfZrTiHo, 2HfZrTiTaY and 2HfZrTiTaHo. Note that the films prepared with the 6Hf, 5HfTa, 4HfZrTa and 3HfZrTiTa target could not be investigated owing to their poor adhesion (delamination) to substrates under the used deposition conditions. The magnetron was driven by a pulsed dc power supply (Rübig MP 120) operating at a repetition frequency of 10 kHz with a deposition-averaged target power of 500 W, and a fixed 50 μs negative-voltage pulse length (duty cycle of 50%) with short-lived (approximately 1 μs) high positive voltage overshoots (300–310 V) after the negative voltage pulses [15]. The base pressure was 1×10^{-3} Pa. The Ar pressure was 0.5 Pa at a gas flow of approximately 25 sccm. The target-to-substrate distance was 100 mm. The substrates were at a floating potential, being highly positive (280–290 V) during the short positive voltage overshoots at the target and negative (close to −10 V) during the negative voltage pulses at the target. The substrate temperature was adjusted to 450 °C using an infrared heater. Let us recall that the possibility to prepare the films on floating substrates (i.e. without any substrate bias) is of key importance for industrial applications.

2.2. Materials characterization

Profilometry (Dektak 8 Stylus Profiler, Veeco) was used to measure the film thickness (1.5–1.9 μm) and the curvature of a Si stripe (4 × 35 mm^2) from which the macrostress, σ, was calculated using the original Stoney's equation [29]. Film hardness, H, and effective Young's modulus, $E^* = E/(1-\nu^2)$, where E and ν are the Young's modulus and the Poisson's ratio, respectively, were measured via an ultra-microindenter (Fischerscope H–100B) according to the ISO 14577–1:2002 E standard with a maximum load of 20 mN. Electrical resistivity, ρ, of the films deposited on Si substrates was measured at room temperature by a standard four-point technique.

The elemental composition of the selected films was measured by wave dispersive spectroscopy (WDS, Thermo Scientific, Magnaray) carried out in a scanning electron microscope (Hitachi, SU-70). The spectra were obtained using a primary energy of 12.5 keV. Modified Proza matrix correction was done using a complex set of references. All the metals (Hf, Zr, Y, Ho, Ti, Ta) were evaluated using appropriate pure metal standards, for boron a BN standard was used (all Astimex Standards Ltd.). Since it is difficult to evaluate the carbon content using WDS, the ratio of atomic concentration of boron and carbon was fixed to a value of 6.5 based on previous measurements (not shown) using glow discharge-optical emission spectroscopy. However, even a big change of this ratio does not significantly vary the ratio of metals. The H, O and Ar contents were fixed at 1, 2 and 3 at.% exploiting our experience with similarly prepared specimens ($Hf_{27}B_{57}C_7$) which were evaluated by the Rutherford backscattering spectroscopy (providing O and Ar contents) and the elastic recoil detection (measuring H content) [13]. Zirconium contamination of Hf portion of composed target is neglected in evaluation since it is lower than 0.5 at.%, Zr content is evaluated obviously only when used as part of composed target. The maximum measurement error for the most abundant element (B) was estimated to be 3 at.%.

The as-deposited films were vacuum annealed in a stainless steel furnace (As-One 100 RTP, Annealsys) up to 1100 °C and 1300 °C. The pressure in the furnace prior to annealing was around 1×10^{-3} Pa. The heating and cooling rates were set at 1 °C/s.

Measurements of X-ray diffraction (XRD) were performed at room temperature in a PANalytical X'Pert PRO MPD diffractometer working in the modified Bragg–Brentano geometry (with an ω-offset of 1.5°) using a CuKα (λ = 0.154187 nm) radiation, 0.25° divergence slit, 0.5° anti-scatter slit, 0.04 rad Soller slits, Ni filter for the CuKβ elimination and an ultrafast semiconductor detector X'Celerator. Samples were scanned over the 2θ-range from 10° to 68° with a scanning speed of 0.071°/s. The data were processed by a PANalytical software package HighScore Plus.

The microstructure of the as-deposited and annealed films was studied on SiC substrates by a Hitachi SU-70 scanning electron microscope (SEM). The energy of the incident electrons was 5 keV.

2.3. Monte-Carlo simulations

Monte-Carlo simulations were used to quantify the energy delivered into the growing films by Ar atoms backscattered (reflected) from the target. First, the backscattering yield of Ar atoms, Y_b, and the initial angular and energy distributions of Ar atoms at the target surface were calculated using the SRIM code [30] for all single metal (Ti, Y, Zr, Ho, Hf and Ta) targets bombarded by Ar^+ ions. Note that the backscattering of Ar atoms from the 85% fraction of B_4C in the target erosion area is negligible. The kinetic energy of Ar^+ ions was assumed to be $\varepsilon = e|U_d|$, where $U_d = -710$ V is the target voltage during a negative voltage pulse. In the second step, the transport of the backscattered argon atoms from the metal part (one metal) of the target (approximately 2000 mm^2) onto the substrate area (20 × 20 mm^2) was characterized using the SIMTRA code [31]. We calculated the transport factor, T_b, determining the fraction of the backscattered Ar atoms striking the substrate area, and the mean energy of the backscattered Ar atoms at the substrate surface, E_{bs}.

The energy delivered into the films per deposited atom by backscattered Ar atoms, E_{bsa}, was determined as a ratio of the total energy of backscattered Ar atoms at the substrate during a deposition using individual composite targets to the corresponding total number of deposited atoms. The total energy of backscattered Ar atoms at the substrate during a deposition using individual composite targets was evaluated using the aforementioned values of Y_b, T_b and E_{bs} calculated for one metal in the target erosion area (see Table 1), and the ion flux Γ_{im} of Ar^+ ions onto the metal part of the target during a negative voltage pulse (duty cycle of 50%). The Γ_{im}, being independent of the target composition, was expressed by the equation

Table 1
The relative mass, m_m [41], and the atomic radius, r_m [42], of the individual target metals, and the backscattering yield of Ar atoms at the target surface, Y_b, calculated for the Ar^+ ions bombarding single metal targets with the kinetic energy of 710 eV. The transport factor T_b determines the fraction of the Ar atoms, backscattered from the metal part of the target, which strike the substrate area, and E_{bs} is the mean energy of the backscattered Ar atoms at the substrate surface.

Target element	Relative mass, m_m	Atomic radius, r_m (pm)	Backscattering yield, Y_b	Transport factor, T_b	Energy of backscattered atoms, E_{bs} (eV)
Ti	47.87	140	0.03	0.0075	12.2
Y	88.91	180	0.12	0.0077	53.3
Zr	91.22	155	0.13	0.0078	54.9
Ho	164.93	175	0.25	0.0079	127.0
Hf	178.49	155	0.26	0.0082	136.5
Ta	180.95	145	0.26	0.0085	137.1

$$\Gamma_{im} = \frac{I_{dm}}{e(1+\gamma)},$$

where I_{dm} is the average discharge current at the metal part of the target during a negative voltage pulse, e is the elementary charge and γ is the ion-induced secondary electron emission yield (assumed to be 0.1 for all target compositions). We put $I_{dm} = 0.15 I_d$, where $I_d = 1.4$ A is the measured average discharge current (independent of the target compositions) during a negative voltage pulse.

The total number of atoms deposited using individual composite targets was calculated from the deposition rate and the volume per atom. The deposition rate is equal to the thickness of 1.5–1.9 μm divided by the deposition time of 100 min. The volume per atom was calculated as a weighted average of those of the corresponding binary diborides (obtained using known lattice constants) and that of the amorphous phase [13] expected to contain the extra B and all C (obtained using their covalent radii and an estimated packing factor of 0.47 [32]).

3. Results and discussion

3.1. Mechanical and electrical properties of as-deposited films

The hardness, H/E^* ratio (measure of resistance to cracking), compressive stress and electrical resistivity of the as-deposited diborides are shown in Fig. 1 as a function of the number of film-metal elements. It can be seen that all films have high hardness (over 30 GPa), high H/E^* ratio (over 0.13) and low electrical resistivity (less than 3.5 μΩ m). The highest hardness (41 GPa), H/E^* ratio (0.16) and σ (3.6 GPa) were all found for the film 5HfTi. Despite the different characteristics of individual metal elements, the figure shows that there is a general trend: increasing the number of metal elements leads to decreasing hardness, H/E^*, compressive stress and electrical conductivity (inverse of presented electrical resistivity). For example, the transition from 2–3 metal elements to 4 metal elements (3HfZrTiY and 3HfZrTiHo) decreases σ from 2.9–3.6 to 2.6–3.1 GPa, and further transition to 5 metal elements (replacement of a part of Hf by Ta) further decreases σ to 1.8–2.0 GPa. Indeed, a case can be made that the enhanced number of metal elements resulting from Ta incorporation is more important for σ than any specific characteristics of Ta: the atomic mass and size of Ta and Hf are very similar, and the Ta-containing films 5HfTa, 4HfZrTa and 3HfZrTiTa together with 6Hf are actually the only ones which delaminated.

The correlation of σ and the energy delivered into the films by backscattered Ar atoms is shown in Fig. 2. Note that investigating this correlation is supported by the fact that the energy delivered into the films by Ar^+ ions is very small (mainly due to a low ionization rate of Ar in the space between the target and the substrate) in the used low-power discharges (target power density averaged over the pulse and the erosion area of only 7.5 Wcm^{-2}). Moreover, this energy of Ar^+ ions is

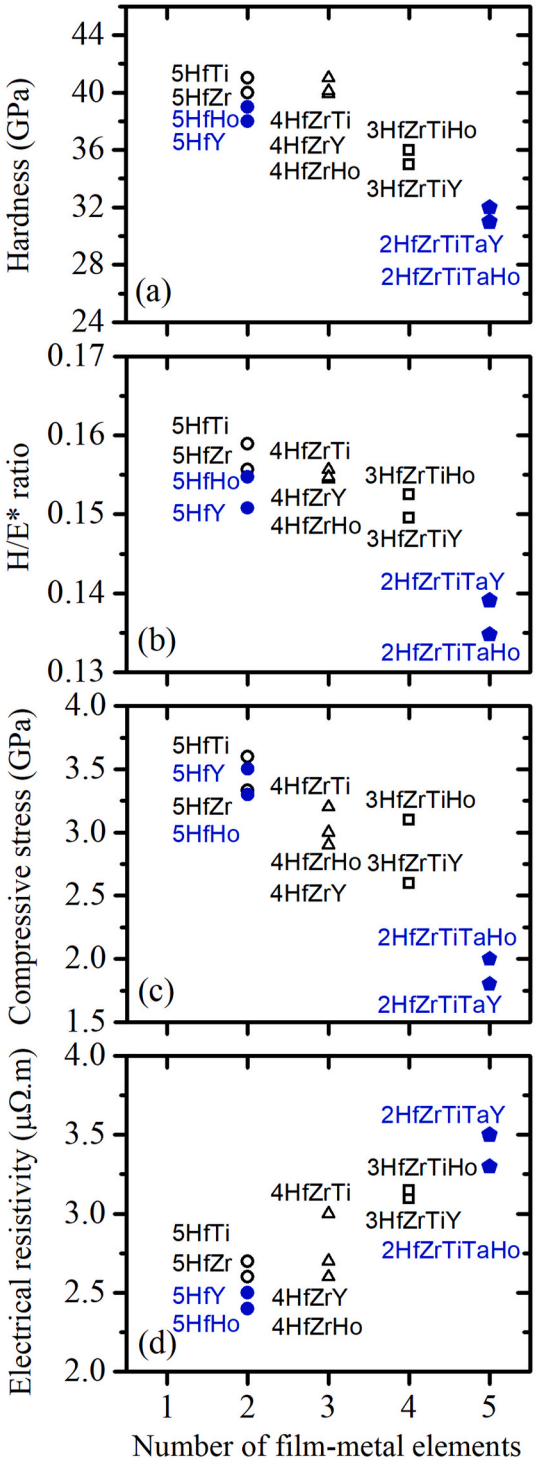

Fig. 1. (a) Hardness, (b) H/E^* ratio, (c) compressive stress and (d) electrical resistivity of the as-deposited films prepared with various target compositions on Si substrates. The labels represent the six metal stripes (2–5 stripes of Hf and 1 stripe per each other metal in the label) covering 6 × 2.5 = 15% of the target erosion area. The films containing 2, 3, 4 and 5 metals are marked by balls, triangles, squares and pentagons, respectively. The films selected for vacuum annealing are marked by full symbols (see Table 2).

almost independent of the target material as indicated by only slight changes in the measured discharge characteristics ($U_d = -710$ V, $I_d = 1.4$ A, the positive voltage overshoot at the target and the floating potential at the substrate, see Sec. 2.1). Fig. 2 shows that E_{bsa} as calculated by the Monte-Carlo simulations is in the range 7.9–12.8 eV/atom and

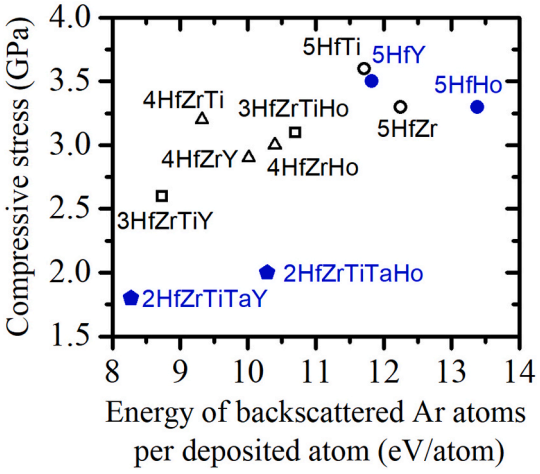

Fig. 2. Relationship between the mean energy of backscattered Ar atoms per deposited atom, E_{bsa}, and the compressive stress, σ, of the as-deposited films prepared with various target compositions on Si substrates. The labels represent the six metal stripes (2–5 stripes of Hf and 1 stripe per each other metal in the label) covering 6 × 2.5 = 15% of the target erosion area. The films containing 2, 3, 4 and 5 metals are marked by balls, triangles, squares and pentagons, respectively. The films selected for vacuum annealing are marked by full symbols (see Table 2).

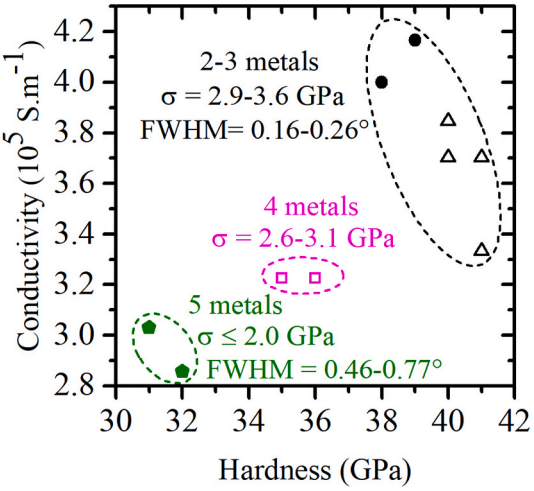

Fig. 3. Relationship between the hardness and the electrical conductivity of the as-deposited films prepared with various target compositions on Si substrates (see Fig. 1). The corresponding ranges of the compressive stress, σ, are given as well. The films containing 2, 3, 4 and 5 metals are marked by balls, triangles, squares and pentagons, respectively. The four films selected for vacuum annealing and X-ray diffraction are marked by full symbols (see Table 2) and the full width at half maximum (FWHM) of the main XRD peak (0001) is given for them.

that it mostly correlates with the mass of target atoms. It can be seen that higher E_{bsa} in most cases leads to higher σ. The films with 5 metals elements 2HfTaTiZrY and especially 2HfTaTiZrHo constitute an exception, as they exhibit σ significantly below the almost linear $\sigma(E_{bsa})$ dependence formed by the rest of the films. While the low σ of 2HfTaTiZrHo may be also due to the high number of metal elements (Fig. 1), the ability of Ho to decrease the compressive stress is clearly demonstrated by the film 5HfHo. First, unlike e.g. 5HfTa, the film 5HfHo did not delaminate. Second, despite the highest E_{bsa} of 12.8 eV/atom, it has σ similar to 5HfZr and even lower than 5HfTi and 5HfY. This ability of Ho to decrease σ may be at least partially due to its large radius, which can make the potentially distorted crystals containing a random mixture of various metal atoms either smaller or less random.

The two main functional properties of interest, namely the (frequently studied) hardness and the (rarely studied for thin film diborides) electrical conductivity, presented separately in Fig. 1, are shown as a function of each other in Fig. 3. It is very important for the application potential of these materials that there is no tradeoff: higher hardness is accompanied by higher conductivity. Furthermore, while there is a tradeoff between high hardness and electrical conductivity (2–3 metal elements) on one side and low compressive stress (5 metal elements) on the other side, it is necessary to emphasize that all presented stress values are relatively low for diboride-based films (let us recall e.g. σ up to 10.5 GPa in Ref. [24]). The figure also quantifies the full width at half maximum (FWHM) of the main XRD peak (surface plane (0001)), indicating (despite the contribution of microstrain) decreasing crystal size when the number of metal elements increases from 2–3 to 5. It is generally accepted that in multicomponent alloys, the electrical conductivity decreases not only due to a different electronic structure (more localized states) but also due to distortions in crystal lattice [33–35]. Quantitatively, increasing number of metal elements from 2–3 through 4 to 5 leads to increasing average atomic-size difference (formula in Ref. [20]) from 0.0–6.0% through 6.2–7.4% to 7.2–8.5%. Furthermore, the electrical conductivity typically decreases due to crystallite size refinement [36]. Hence, the lower conductivity of compositions with 5 metal elements is consistent with the wider XRD peaks and with the possible higher number of defects in the atomic and electronic structure. In parallel, although lower crystallite size should result in higher hardness according to Hall-Petch strengthening mechanism, many studies have shown that reverse Hall-Petch effect can occur when the crystallite size becomes smaller than a critical value [37]. Furthermore, a decrease in the number of covalent bonds at finer crystallite size was reported to be the main reason for lower hardness of SiC [38]. Hence, the lower hardness of compositions with 5 metal elements is consistent not only with the lower compressive stress but also, again, with the lower crystal size.

In order to compare the thermal stabilities of so-called high-entropy diborides (5 metal elements) with that of low-entropy diborides (2 metal elements), four compositions including 2HfZrTiTaY, 2HfZrTiTaHo, 5HfY and 5HfHo (full symbols in Figs. 1–3) were selected for further and deeper analyses (see Table 2). The Y- and Ho-containing compositions were selected because these two elements are different from Hf both in terms of size (contrary to similarly large Ta and Zr) and in terms of periodic group number (contrary to Ti and Zr). This size mismatch does, for example, prevent a formation of stable disordered $Hf_{0.5}Y_{0.5}B_2$ solid solution according to Ref. [1]. At the same time, Y and Ho have similar atomic radii but significantly different atomic masses (Table 1), allowing one to check whether the thermal stability is independent of the latter.

3.2. Thermal stability of film structures and properties

The elemental composition of the four selected samples 2HfZrTiTaY, 2HfZrTiTaHo, 5HfY and 5HfHo was quantified (Table 1), and their thermal stability was analyzed by vacuum annealing to 1100 °C and 1300 °C. The changes of their hardness, H/E^*, electrical resistivity and FWHM of the main XRD peak are shown in Fig. 4. Despite the relaxation

Table 2
Elemental composition of the selected films and their adhesion to Si and SiC substrates after annealing in vacuum up to 1100 °C and 1300 °C, respectively.

Target metals	Film composition (at.%)	Film adhesion after annealing	
		Si (1100 °C)	SiC (1300 °C)
5HfY	$Hf_{22}Y_5B_{58}C_9$	Good	Cracked film
5HfHo	$Hf_{22}Ho_5B_{58}C_9$	Good	Cracked film
2HfZrTiTaY	$Hf_8Zr_4Ti_4Ta_4Y_5B_{60}C_9$	Good	Good
2HfZrTiTaHo	$Hf_{10}Zr_4Ti_4Ta_4Ho_5B_{58}C_9$	Good	Good

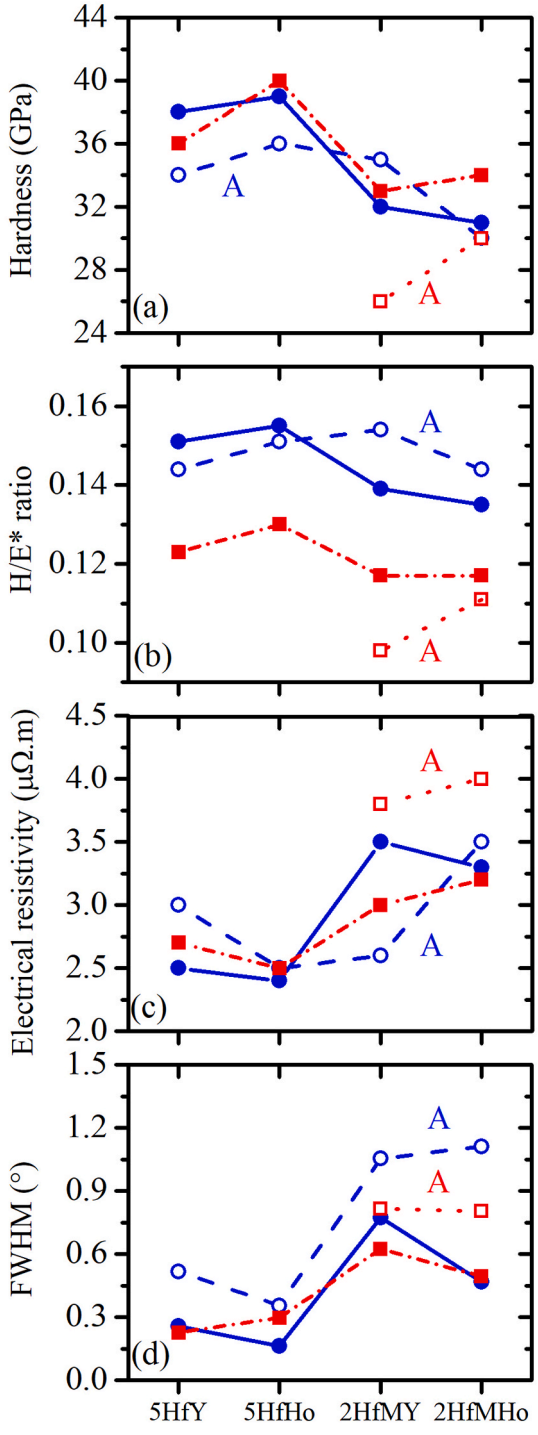

Fig. 4. (a) Hardness, (b) H/E^* ratio, (c) electrical resistivity and (d) full width at half maximum of the (0001) XRD patterns of the selected films (see Table 2; M = ZrTiTa) on Si substrates before (full circles) and after (A, empty circles) annealing in vacuum up to 1100 °C, and on SiC substrates before (full squares) and after (A; empty squares; shown only for two multicomponent films with good adhesion) annealing in vacuum up to 1300 °C.

of σ (see below), all four films exhibit good thermal stability of hardness when annealed to 1100 °C. The hardness of 5HfY and 5HfHo decreased by only ≈4 GPa, the decrease of hardness of 2HfZrTiTaHo is negligible, and the hardness of 2HfZrTiTaY even increased from 32 to 35 GPa. A case can be made that the effect of stress relaxation is (more than) compensated by annihilation of defects (reported e.g. for ZrB_2-rich materials at 800 °C in Ref. [17]). However, after annealing to 1300 °C, the samples 5HfY and 5HfHo were delaminated and the hardness of 2HfZrTiTaY and 2HfZrTiTaHo decreased from 31 to 26 GPa and from 33 to 30 GPa, respectively.

Regarding the H/E^* ratio, it must be noted that it is systematically lower for the films on SiC owing to a higher E^*. It can be seen that the films with 5 metal elements perform better not only in terms of H but also in terms of H/E^*. After annealing to 1100 °C, this ratio slightly decreases for 5HfY and 5HfHo whereas it increases from 0.135–0.139 to 0.144–0.154 for 2HfZrTiTaY and 2HfZrTiTaHo. However, annealing of 2HfZrTiTaY and 2HfZrTiTaHo to 1300 °C leads not only to lower H but also to lower H/E^*.

The electrical resistivities of the films deposited on SiC and Si are rather similar. The changes of electrical resistivity after annealing to 1100 °C do not follow a unique trend (the largest difference observed is lower resistivity of 2HfZrTiTaY), while the resistivity of 2HfZrTiTaY and 2HfZrTiTaHo increases after annealing to 1300 °C. However, the increase of the electrical resistivity is small (factor of ≈1.25; let alone that it may be partially explained by a slight surface oxidation) and the films preserve their metal-like character.

The width of the main (0001) XRD peak quantified in Fig. 4d is complemented by whole XRD patterns on Si and SiC before and after annealing shown in Fig. 5. The standard XRD patterns of comprising diborides (PDF card numbers [39] HfB_2, 00-038-13; ZrB_2, 00-034-04; TiB_2, 00-035-0741; TaB_2, 00-038-1462; YB_2, 04-004-1054; HoB_2, 00-026-0739) and HfO_2 (00-053-0560) are shown as well. All as-deposited films exhibit only one AlB_2-type crystalline phase with strongly preferred (0001) orientation. After annealing to 1100 °C, this textured structure does not change (except a very small HfO_2 peak in the case of 5HfHo) but all diboride peaks are shifted towards right hand side (implying relaxation of the compressive stress and the macrostrain) and FWHM of the main (0001) peak systematically increases for all samples. The structures of the films 2HfZrTiTaY and 2HfZrTiTaHo remain stable even after annealing to 1300 °C: the peaks once again shift to the right but they remain (or, after a closer look, become even slightly more) symmetrical, indicating that no decomposition of the diborides takes place. Furthermore, the peaks obtained after annealing to 1300 °C are wider compared to as-deposited samples, but actually narrower compared to those obtained after annealing to 1100 °C. Note that a similar peak broadening resulting from annealing to the same temperature of 1300 °C was reported for (HfTaVWZr)-diborides in Ref. [21].

While the peak broadening cannot be explained by a crystal decomposition, it may be explained by recrystallization (better known for metals), i.e. nucleation and subsequent growth of new strain-free crystals of the same phase from the parent crystals. Although the melting temperature of diborides is quite high (over 3000 °C) and the annealing temperature of 1300 °C is therefore below the homologous temperature, recrystallization of diborides prepared by magnetron sputtering can occur at temperatures as low as 800 °C due to dislocations and other defects [17]. When a recrystallization is either stopped at the beginning or carried out at a low temperature, it can lead to finer grain size [40]. This is the way how the annealing to 1100 °C can lead to increased FWHM (some of the new crystals are small because they represent the initial stage of recrystallization, i.e. the distribution of sizes of all crystals is wider) than the annealing to 1300 °C.

The high-temperature phase stability of the films 2HfZrTiTaY and 2HfZrTiTaHo (compared to 5HfY and 5HfHo) can be attributed to the entropic effect resulting from the presence of 5 metal elements in the metal sublattice. The entropy calculated for these materials using their exact compositions $Hf_8Zr_4Ti_4Ta_4Y_5B_{60}C_9$ and $Hf_{10}Zr_4Ti_4Ta_4Ho_5B_{58}C_9$ is −1.57R and −1.54R, respectively, per metal atom in their crystalline part. This categorizes these materials as high-entropy metal sublattice diborides (HESB) [21]. Similar entropic stabilization of ternary solid solutions of YB_2 with HfB_2, TaB_2 or TiB_2 is discussed in Ref. [1]. Furthermore, the SEM fracture cross-sections of these two films show very dense, pinhole free, and nearly featureless growth morphology both before and after annealing to 1300 °C (Fig. 6).

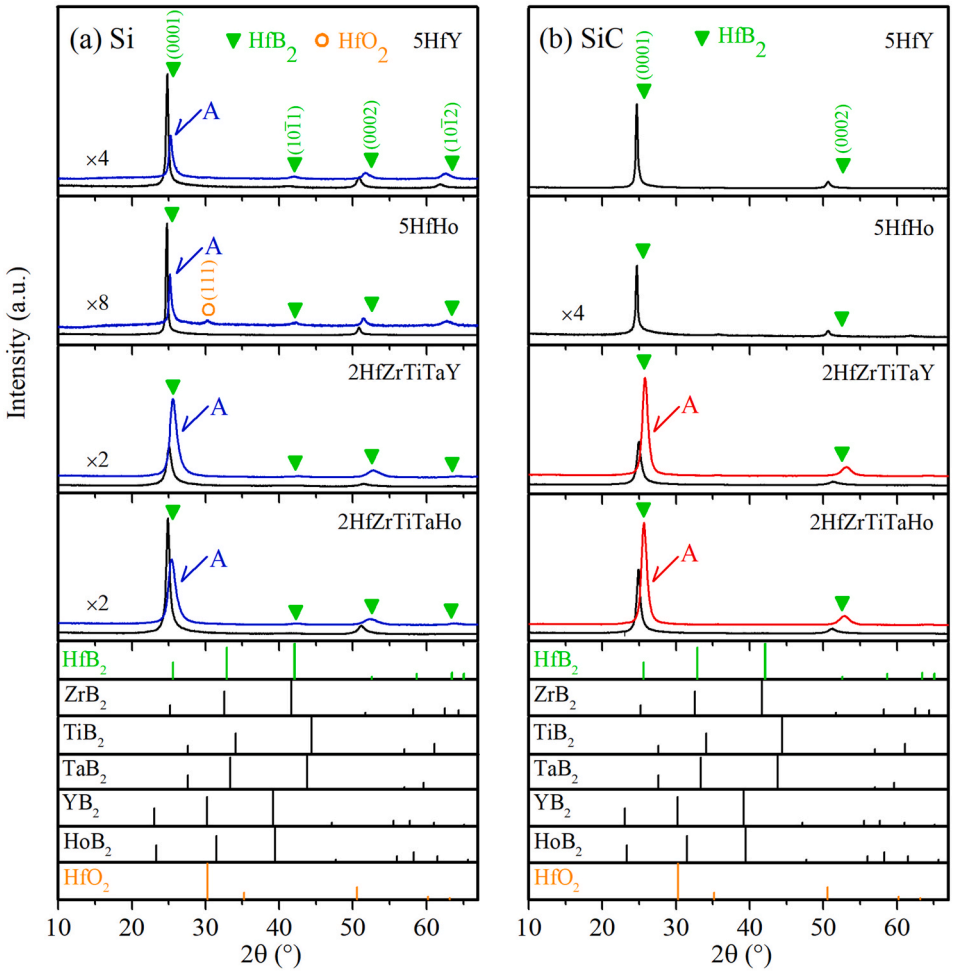

Fig. 5. X-ray diffraction patterns taken from the selected films (see Table 2) on (a) Si substrates before and after (A) annealing in vacuum up to 1100 °C, and (b) SiC substrates before and after (A, shown only for two multicomponent films with good adhesion) annealing in vacuum up to 1300 °C. Theoretical positions of the main diffraction peaks of HfB_2, ZrB_2, TiB_2, TaB_2, YB_2, HoB_2 and HfO_2 are marked.

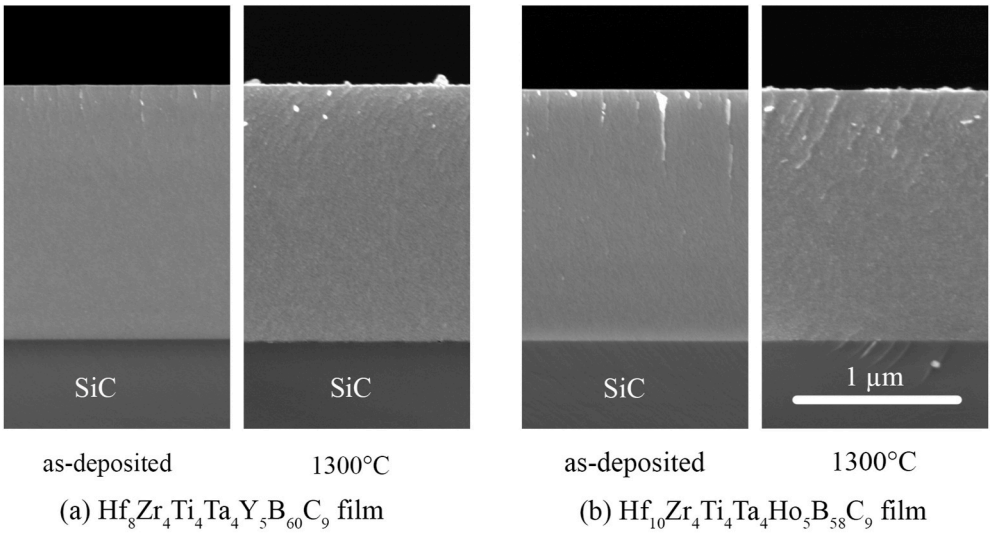

Fig. 6. SEM fracture cross-sections of the (a) $Hf_8Zr_4Ti_4Ta_4Y_5B_{60}C_9$ film and (b) $Hf_{10}Zr_4Ti_4Ta_4Ho_5B_{58}C_9$ film on SiC substrates before and after annealing in vacuum up to 1300 °C.

4. Conclusions

HfB_2-based thin-film materials were prepared by an industry-friendly deposition technique: pulsed magnetron sputtering of easy-to-sputter B_4C-based targets with substrates at a floating potential. Structure, hardness (31–41 GPa), hardness-to-effective Young's modulus ratio (0.13–0.16), electrical conductivity (2.8–4.2 × 10^5 S m^{-1}) and thermal stability of the films was studied in a wide compositional range resulting from a partial replacement of Hf with other elements (Ti, Y, Zr, Ho or Ta). Growing number of metal elements from 2 to 5 leads to decreasing crystal size, strongly decreasing compressive stress and slightly decreasing hardness and electrical conductivity. The compressive stress is largely correlated with the energy delivered into the films, varied mainly because of varied mass of target metal atoms. Hard and conductive high-entropy septenary compositions $Hf_8Zr_4Ti_4Ta_4Y_5B_{60}C_9$ and $Hf_{10}Zr_4Ti_4Ta_4Ho_5B_{58}C_9$ which exhibit particularly low compressive stress of $\leq$2 GPa and nearly perfect thermal stability of their phase structure (single AlB_2-type crystalline phase) and microstructure up to at least 1300 °C have been identified. The results are important for the design of thin-film materials combining multiple functional properties for various technological applications, and the design of pathways for their scalable preparation.

Declaration of competing interest

The authors declare that they have no known competing financial interests or personal relationships that could have appeared to influence the work reported in this paper.

Acknowledgment

This work was supported by the Grant Agency of the Czech Republic under Project No. 19-14011S.

References

[1] B. Alling, H. Hogberg, R. Armiento, J. Rosen, L. Hultman, A theoretical investigation of mixing thermodynamics, age-hardening potential, and electronic structure of ternary $M(1)_{1-x}M(2)_xB_2$ alloys with AlB_2 type structure, Sci. Rep. 5 (2015) 9888, https://doi.org/10.1038/srep09888.

[2] W.G. Fahrenholtz, G.E. Hilmas, I.G. Talmy, J.A. Zaykoski, Refractory diborides of zirconium and hafnium, J. Am. Ceram. Soc. 90 (2007) 1347–1364, https://doi.org/10.1111/j.1551-2916.2007.01583.x.

[3] M. Zhang, X. Ma, J. Yin, Y. Zhang, L. Zhang, J. Wen, L. Dai, R. Kuang, H. Chen, X. Weng, X. Zhao, D. Liang, J. Xie, L. Deng, Microstructure, infrared optical properties and thermal stability of ZrB_2 and double-layer-structure Al_2O_3/ZrB_2 thin films by magnetron sputtering technique, Appl. Surf. Sci. 532 (2020) 147280, https://doi.org/10.1016/j.apsusc.2020.147280.

[4] Y. Shen, J. Jiang, P. Zeman, M. Kotrlová, V. Šímová, J. Vlček, E.I. Meletis, Microstructure of high temperature oxidation resistant $Hf_6B_{10}Si_{31}C_2N_{50}$ and $Hf_7B_{10}Si_{32}C_2N_{44}$ films, Coat 10 (2020) 1–17, https://doi.org/10.3390/coatings10121170.

[5] B.R. Golla, A. Mukhopadhyay, B. Basu, S.K. Thimmappa, Review on ultra-high temperature boride ceramics, Prog. Mater. Sci. 111 (2020) 100651, https://doi.org/10.1016/j.pmatsci.2020.100651.

[6] G.-J. Zhang, D.-W. Ni, J. Zou, H.-T. Liu, W.-W. Wu, J.-X. Liu, T.S. Suzuki, Y. Sakka, Inherent anisotropy in transition metal diborides and microstructure/property tailoring in ultra-high temperature ceramics—a review, J. Eur. Ceram. Soc. 38 (2018) 371–389, https://doi.org/10.1016/j.jeurceramsoc.2017.09.012.

[7] J.F. Guria, A. Bansal, V. Kumar, Effect of additives on the thermal conductivity of zirconium diboride based composites – a review, J. Eur. Ceram. Soc. 41 (2021) 1–23, https://doi.org/10.1016/j.jeurceramsoc.2020.08.051.

[8] B. Bakhit, J. Palisaitis, J. Thörnberg, J. Rosen, P.O.Å. Persson, L. Hultman, I. Petrov, J.E. Greene, G. Greczynski, Improving the high-temperature oxidation resistance of TiB_2 thin films by alloying with Al, Acta Mater. 196 (2020) 677–689, https://doi.org/10.1016/j.actamat.2020.07.025.

[9] N. Nedfors, O. Vozniy, J. Rosen, Effect of synchronized bias in the deposition of TiB_2 thin films using high power impulse magnetron sputtering, J. Vac. Sci. Technol. A 36 (2018), 031510, https://doi.org/10.1116/1.5003194.

[10] V. Šroba, T. Fiantok, M. Truchlý, T. Roch, M. Zahoran, B. Grančič, P. Švec, Š. Nagy, V. Izai, P. Kúš, M. Mikula, Structure evolution and mechanical properties of hard tantalum diboride films, J. Vac. Sci. Technol. A 38 (2020), 033408, https://doi.org/10.1116/6.0000155.

[11] A. Chatterjee, A.A. Polycarpou, J.R. Abelson, P. Bellon, Nanoscratch study of hard HfB_2 thin films using experimental and finite element techniques, Wear 268 (2010) 677–685, https://doi.org/10.1016/j.wear.2009.11.001.

[12] W. Dai, X. Gao, X. Li, Q. Wang, Influence of carbon incorporation on microstructure and properties of titanium diboride coatings deposited by combining ion beam with magnetron sputtering, Ceram. Int. 45 (2019) 22498–22505, https://doi.org/10.1016/j.ceramint.2019.07.273.

[13] J. Kohout, J. Vlček, J. Houška, P. Mareš, R. Čerstvý, P. Zeman, M. Zhang, J. Jiang, E.I. Meletis, T. Zuzjaková, Hard multifunctional Hf-B-Si-C films prepared by pulsed magnetron sputtering, Surf. Coating. Technol. 257 (2014) 301–307, https://doi.org/10.1016/j.surfcoat.2013.12.007.

[14] M. Zhang, J. Jiang, P. Mareš, J. Houška, J. Vlček, E.I. Meletis, Effect of the Si content on the microstructure of hard, multifunctional Hf-B-Si-C films prepared by pulsed magnetron sputtering, Appl, Surf. Sci. 357 (2015) 1343–1354, https://doi.org/10.1016/j.apsusc.2015.09.249.

[15] P. Mareš, J. Vlček, J. Houška, J. Kohout, J. Čapek, Effect of energetic particles on pulsed magnetron sputtering of hard nanocrystalline MBCN (M = Ti, Zr, Hf) films with high electrical conductivity, Thin Solid Films 688 (2019) 137334, https://doi.org/10.1016/j.tsf.2019.05.053.

[16] B. Bakhit, D.L.J. Engberg, J. Lu, J. Rosen, H. Högberg, L. Hultman, I. Petrov, J. E. Greene, G. Greczynski, Strategy for simultaneously increasing both hardness and toughness in ZrB_2-rich $Zr_{1-x}Ta_xB_y$ thin films, J. Vac. Sci. Technol. A 37 (2019), 031506, https://doi.org/10.1116/1.5093170.

[17] B. Bakhit, J. Palisaitis, Z. Wu, M.A. Sortica, D. Primetzhofer, P.O.Å. Persson, J. Rosen, L. Hultman, I. Petrov, J.E. Greene, G. Greczynski, Age hardening in superhard ZrB_2-rich $Zr_{1-x}Ta_xB_y$ thin films, Scripta Mater. 191 (2021) 120–125, https://doi.org/10.1016/j.scriptamat.2020.09.026.

[18] B. Bakhit, S. Dorri, A. Kooijman, Z. Wu, J. Lu, J. Rosen, J.M.C. Mol, L. Hultman, I. Petrov, J.E. Greene, G. Greczynski, Multifunctional ZrB_2-rich $Zr_{1-x}Cr_xB_y$ thin films with enhanced mechanical, oxidation, and corrosion properties, Vacuum 185 (2021) 109990, https://doi.org/10.1016/j.vacuum.2020.109990.

[19] B. Grančič, M. Pleva, M. Mikula, M. Čaplovičová, L. Satrapinskyy, T. Roch, M. Truchlý, M. Sahul, M. Gregor, P. Švec, M. Zahoran, P. Kúš, Stoichiometry, structure and mechanical properties of co-sputtered $Ti_{1-x}Ta_xB_{2\pm\Delta}$ coatings, Surf. Coating. Technol. 367 (2019) 341–348, https://doi.org/10.1016/j.surfcoat.2019.04.017.

[20] J. Gild, Y. Zhang, T. Harrington, S. Jiang, T. Hu, M.C. Quinn, W.M. Mellor, N. Zhou, K. Vecchio, J. Luo, High-entropy metal diborides: a new class of high-entropy materials and a new type of ultrahigh temperature ceramics, Sci. Rep. 6 (2016) 37946, https://doi.org/10.1038/srep37946.

[21] A. Kirnbauer, A. Wagner, V. Moraes, D. Primetzhofer, M. Hans, J.M. Schneider, P. Polcik, P.H. Mayrhofer, Thermal stability and mechanical properties of sputtered (Hf,Ta,V,W,Zr)-diborides, Acta Mater. 200 (2020) 559–569, https://doi.org/10.1016/j.actamat.2020.09.018.

[22] P.H. Mayrhofer, A. Kirnbauer, P. Ertelthaler, C.M. Koller, High-entropy ceramic thin films; A case study on transition metal diborides, Scripta Mater. 149 (2018) 93–97, https://doi.org/10.1016/j.scriptamat.2018.02.008.

[23] C. Oses, C. Toher, S. Curtarolo, High-entropy ceramics, Nat. Rev. Mater. 5 (2020) 295–309, https://doi.org/10.1038/s41578-019-0170-8.

[24] A. Goncharov, P. Ignatenko, V. Konovalov, V. Stupak, G. Volkova, V. Glazunova, V. Petukhov, Phase formation, structure, and state of stress of nanostructured tantalum boride films, Phys. Met. Metallogr. 103 (2007) 77–82, https://doi.org/10.1134/S0031918X07010103.

[25] V.A. Konovalov, D.N. Terpiy, Growth kinetics and properties of nanostructured hafnium diboride films, Tech. Phys. 54 (2009) 1023–1026, https://doi.org/10.1134/s1063784209070160.

[26] O. Paris, D. Lang, J. Li, P. Schumacher, M. Deluca, R. Daniel, M. Tkadletz, N. Schalk, C. Mitterer, J. Todt, J. Keckes, Z. Zhang, G. Fritz-Popovski, C. Ganser, C. Teichert, H. Clemens, Complementary high spatial resolution methods in materials science and engineering, Adv. Eng. Mater. 19 (2017) 1600671, https://doi.org/10.1002/adem.201600671.

[27] C. Mitterer, Borides in thin film technology, J. Solid State Chem. 133 (1997) 279–291, https://doi.org/10.1006/jssc.1997.7456.

[28] J. Vlček, Š. Potocký, J. Čížek, J. Houška, M. Kormunda, P. Zeman, V. Peřina, J. Zemek, Y. Setsuhara, S. Konuma, Reactive magnetron sputtering of hard Si-B-C-N films with a high-temperature oxidation resistance, J. Vac. Sci. Technol. A 23 (2005) 1513–1522, https://doi.org/10.1116/1.2049298.

[29] J. Gunnars, U. Wiklund, Determination of growth-induced strain and thermo-elastic properties of coatings by curvature measurements, Mater. Sci. Eng. A 336 (2002) 7–21, https://doi.org/10.1016/S0921-5093(01)01979-7.

[30] J. Biersack, W. Eckstein, Sputtering studies with the Monte Carlo program TRIM. SP, Appl. Phys. A 34 (1984) 73–94, https://doi.org/10.1007/BF00614759.

[31] K. Van Aeken, S. Mahieu, D. Depla, The metal flux from a rotating cylindrical magnetron: a Monte Carlo simulation, J. Phys. D Appl. Phys. 41 (2008) 205307, https://doi.org/10.1088/0022-3727/41/20/205307.

[32] M. Matas, M. Prochazka, J. Vlcek, J. Houska, Dependence of characteristics of Hf (M)SiBCN (M = Y, Ho, Ta, Mo) thin films on the M choice: Ab-initio and experimental study, Acta Mater. 206 (2021) 116628, https://doi.org/10.1016/j.actamat.2021.116628.

[33] G. Anand, A.P. Wynn, C.M. Handley, C.L. Freeman, Phase stability and distortion in high-entropy oxides, Acta Mater. 146 (2018) 119–125, https://doi.org/10.1016/j.actamat.2017.12.037.

[34] Y. Yang, L. Ma, G.-Y. Gan, W. Wang, B.-Y. Tang, Investigation of thermodynamic properties of high entropy (TaNbHfTiZr)C and (TaNbHfTiZr)N, J. Alloys Compd. 788 (2019) 1076–1083, https://doi.org/10.1016/j.jallcom.2019.02.254.

[35] E. Lewin, Multi-component and high-entropy nitride coatings—a promising field in need of a novel approach, J. Appl. Phys. 127 (2020) 160901, https://doi.org/10.1063/1.5144154.
[36] L. Wei, Z. Lin-Li, Z. Xiao-Jing, Grain size effect on electrical conductivity and giant magnetoresistance of bulk magnetic polycrystals, Chin. Phys. Lett. 26 (2009) 117502, https://doi.org/10.1088/0256-307x/26/11/117502.
[37] B. Ratzker, A. Wagner, M. Sokol, L. Meshi, S. Kalabukhov, N. Frage, Deformation in nanocrystalline ceramics: a microstructural study of $MgAl_2O_4$, Acta Mater. 183 (2020) 137–144, https://doi.org/10.1016/j.actamat.2019.11.015.
[38] C. Pan, L. Zhang, W. Jiang, W. Setyawan, L. Chen, Z. Li, N. Liu, T. Wang, Grain size dependence of hardness in nanocrystalline silicon carbide, J. Eur. Ceram. Soc. 40 (2020) 4396–4402, https://doi.org/10.1016/j.jeurceramsoc.2020.05.060.
[39] JCPDS-ICDD, PDF-4+ Database, International Centre For Diffraction Data, Newton Square, PA, USA, 2020.
[40] S.F. Liu, Y.H. Liu, L.J. Li, C. Deng, H.Y. Fan, Y. Guo, L.F. Cao, Q. Liu, Effects of pre-recovery on the recrystallization microstructure and texture of high-purity tantalum, J. Mater. Sci. 53 (2017) 2985–2994, https://doi.org/10.1007/s10853-017-1732-z.
[41] J.R. De Laeter, J.K. Böhlke, P. De Bievre, H. Hidaka, H. Peiser, K. Rosman, P. Taylor, Atomic weights of the elements. Review 2000 (IUPAC technical report), Pure Appl. Chem. 75 (2003) 683–800, https://doi.org/10.1351/pac200375060683.
[42] J.C. Slater, Atomic radii in crystals, J. Chem. Phys. 41 (1964) 3199–3204, https://doi.org/10.1063/1.1725697.